ORCA – Online Research @ Cardiff

Metal-Organic Coordination Networks on a Titanium Carbide MXene:

DFT Based Grand Canonical Monte Carlo Simulation

Vitaly A. Gorbunov [a,], Anastasiia I. Uliankina [a], Pavel V. Stishenko [a,b], and Alexander V. Myshlyavtsev [a]*

[a] Omsk State Technical University, 11 Mira, Omsk, 644050, Russian Federation

[b] Cardiff Catalysis Institute, School of Chemistry, Cardiff University, Cardiff, United Kingdom

Corresponding author: vitaly_gorbunov@mail.ru

Abstract

The self-assembly of 2D metal-organic networks comprising 1,3,5-tris (pyridyl)benzene (TPyB) molecules and copper atoms on the oxygen-terminated titanium carbide MXene surface was theoretically investigated. We have developed a lattice model of the TPyB-Cu networks on the energetically heterogeneous $Ti_2CO_2(0001)$ surface. The model based on DFT calculations of the structure and energy of key adsorption complexes and metal-organic structures. Using the grand canonical Monte Carlo method, we have calculated and analyzed adsorption isotherms, structure, potential energy, and heat capacity of the adlayer. Due to steric hindrances in the three-fold Cu-TPyB junction, metal-organic structures consisting of only two-fold Cu-TPyB coordination motifs predominantly emerge on the $Ti_2CO_2(0001)$ surface: honeycomb (HON), honeycomb filled with Cu_3TPyB (HON + Cu_3TPyB) and zigzag (ZZ) phases. These phases differ in the local environment of the copper adatoms. Thermal stability of the phases decreases in the following series: ZZ, HON + Cu_3TPyB and HON. Self-assembly of these structures offers the opportunity to stabilize and "tune" properties of the single-atom $Cu/Ti_2CO_2(0001)$ catalyst. We hope that our results will stimulate further experimental studies of hybrid "metal-organic network/MXene" catalysts.

28   **1. Introduction**

29   Population growth and consequently increased energy consumption as well as global

30   environmental pollution require new clean and sustainable energy conversion technologies. Important

31   role in solving these problems is played by highly efficient and inexpensive electrocatalysts for proton

32   exchange membrane fuel cells and metal-air batteries [1–6]. The bottleneck of these devices are catalytic

33   oxygen reduction (ORR) and oxygen evolution (OER) reactions, which are relatively slow [7–10]. Today,

34   expensive catalysts containing noble metals and their oxides are used to catalyze ORR/OER reactions

35   [1,8,11,12]. A promising alternative is supported single- and double-atom catalysts based on transition

36   metals [9,10,13–20] and carbon materials [6,7,21–23]. Single-atom catalysts (SACs), where metal atoms

37   are dispersed on an optimal substrate, show extremely high utilization efficiency of the active component

38   surface. SACs are inherently characterized by uniform active sites with high selectivity for specific

39   reactions. The unique electronic structure and coordination environment of the active sites in SACs make

40   it possible to fine-tune the adsorption energy of reactants, products, and intermediates influencing the

41   activity and selectivity of the catalytic process.

42   The catalysts based on iron and copper supported by a porous carbon doped with nitrogen and/or

43   containing pyridine groups are known to be one of the most active ORR catalysts [6,18,22–31]. In these

44   cases, the catalytic active site is an iron or copper adatom coordinated with four nitrogen atoms. However,

45   this coordination structure does not provide the optimized binding energy for ORR/OER intermediates

46   and thus the catalytic activity [9]. Introducing O atom into coordination environment of the metal center

47   can be applied to tune the electronic structure and change the catalytic activity and selectivity of SACs

48   [9,32,33]. Unfortunately, the stability of such carbon supported catalysts is poor.

49   Recently, transition metal single- and double-atom catalysts supported by N- and C-based MXenes

50   are shown to exhibit similar activity and increased stability in ORR/OER reactions [5,13,34–39]. In the

51   paper [5] the Ti_2CO_2-supported non-noble Cu SAC is found to exhibit excellent ORR activity. However, an

52   open question remains about stability of such SAC. The point is that the cohesion energy of copper is

53   greater than the calculated binding energy of the copper atom with $Ti_2CO_2(0001)$ surface. Therefore, the

54   aggregation of the copper atoms on the MXene surface is possible. According to M. Keyhanian et al [40],

55 the diffusion barrier for Cu atoms on the $Ti_2CO_2(0001)$ surface is approximately 27 kJ/mol, or 14% of the

56 adsorption energy. This is one of the lowest diffusion barriers in the first row of transition metals.

57 Nevertheless, the aggregation can be kinetically hampered.

58   Combining the electroconductive MXenes with metal-organic frameworks (MOFs) having tunable

59 porosity, and diversity of metal sites and functional groups could significantly improve the catalytic

60 activity, selectivity and especially stability of such hybrid materials in ORR/OER [41,42]. Let us give some

61 examples. L. Zhao et al had synthesized the CoBDC/terminated titanium carbide hybrid catalyst [43]. In

62 this case, the catalyst is MXene sheets coated with a few nanometers thick CoBDC layer. Metal-organic

63 frameworks, namely ZIF-67 based on cobalt, nickel, and imidazole, can be deposited on the MXene Ti_3C_2

64 surface in the form of nanoparticles several hundred nm in size [41,44]. In both cases, the high porosity

65 of MOF provides good mass transfer and large surface area of the active component, while the MXene

66 provides the electroconductivity of the catalyst. The oxidation state of the metal center does not change

67 after hybridization with MXene. The synthesized hybrid catalysts show high activity in OER and NRR

68 reactions. A negative effect of the MXene surface in the hybrid Co,Ni-MOF/MXene catalysts on the

69 catalytic activity in OER is also observed [45]. Since the chemical environment of the metal center in the

70 hybrid catalyst remains practically unchanged, the authors believe that the reduced OER activity of the

71 material is associated with the electron-donor properties of the MXene. The reduced oxidation states of

72 nickel and cobalt in the hybrid catalyst corroborate this hypothesis. MOF layers deposited on MXene

73 surfaces were also used as a precursor of the active component in ORR/OER. For example, a hybrid

74 NiCoS/MXene catalyst for OER was synthesized by depositing a ZIF-67 layer onto the terminated titanium

75 carbide surface, followed by treatment with nickel nitrate and sulfuration [46]. Strong interaction

76 between the NiCoS and MXene surface significantly affects the electronic structure of the catalytic active

77 site. Such interaction promotes charge transfer from the sulfide to the conductive MXene and thus

78 increases the catalytic activity in OER. In recent paper, H. Zhang et al [47] had investigated the self-

79 assembly of amorphous Ni-MOF nanospheres on MXenes. The MOF nanospheres anchored on the MXene

80 surface were subsequently conversed into porous nanospheres of catalytically active nickel phosphate

81 through the etching with potassium dihydrogenphosphate. Direct bonding between nickel phosphate

82   nanospheres and MXene surface enables the fast electron transfer, addressing the low conductivity of

83   nickel phosphate. The works briefly discussed above give us reason to believe that coupling of MOF and

84   MXenes is an effective strategy to tune the activity, selectivity and stability of the ORR/OER catalysts.

85   Experimentally, several synthesis approaches to the of Cu SACs have been proposed to avoid the

86   aggregation of copper atoms [48–50]. In this theoretical work, we have evaluated the possibility of

87   stabilizing copper single atoms on the oxygen-terminated titanium carbide surface through the self-

88   assembly of a surface-confined metal-organic network comprising 1,3,5-tris(pyridyl)benzene molecules

89   and copper atoms (TPyB-Cu). Unlike the works mentioned above, each copper atom in the TPyB-Cu metal-

90   organic network on the Ti_2CO_2(0001) surface is assumed to be potentially bound both to oxygen atoms of

91   the MXene surface and to a different number of pyridyl nitrogen atoms. We believe that self-assembly of

92   different TPyB-Cu metal-organic networks on the Ti_2CO_2(0001) surface can be an effective tool to control

93   the N/C/O-coordination environment of the Cu atom. In the light of the facts discussed above, such hybrid

94   catalyst can potentially be assumed to have a high electrical conductivity, activity, and stability in

95   ORR/OER. There are many different phases can emerge in the TPyB-Cu metal-organic layer on Au (111)

96   surface [51–54]. All these phases differ in the surface concentration of various copper sites: isolated

97   atoms, condensed clusters, two- and three-fold TPyB-Cu coordination motifs. Electronic structure of these

98   Cu active sites is obviously different. It can be assumed that the catalytic properties of these Cu sites also

99   differ. Thus, whether emergence of such metal-organic structures on the Ti_2CO_2(0001) surface possible or

100   not is the question of fundamental importance. The positive answer will open the possibility of "tuning"

101   the catalytic properties of the Cu/Ti_2CO_2 system.

102   Today, the task of development of new surface-confined metal-organic structures is mainly solved

103   by trial and error. Even small changes under experimental conditions lead to significant changes in the

104   structure of the metal-organic layer [52,55,56]. For this reason, molecular simulation methods are widely

105   used to study the self-assembly of such systems. A detailed theoretical description of complex metal-

106   organic networks on the solid surface is also complicated and time-consuming. One of the possible

107   strategies to solve this problem is development of coarse-grained models, in particular lattice models, of

108   such systems and studying them using the Monte Carlo methods [54,57–63]. Locally regular geometry of

109   the coordination bonds and their relative rigidity make the lattice models a natural tool for investigations

110   in this case.

111   The aim of this work is to answer question: whether the self-assembly of stable TPyB-Cu metal-

112   organic networks on the O-terminated titanium carbide MXene surface possible or not? To achieve this,

113   we have developed the lattice model of the metal-organic layer based on our electron density functional

114   theory (DFT) calculations and further performed the simulations using grand canonical Monte Carlo

115   method. The model of TPyB-Cu/Ti_2CO_2 self-assembly adopts several assumptions following from the STM

116   studies of the adsorption layers consisting of TPyB molecules and copper atoms, as well as from our DFT

117   calculations of the geometries of the adsorption complexes and binding energies of the components with

118   the $Ti_2CO_2(0001)$ surface.

119

120   **2. Details of DFT calculations**

121   The geometry and bonding energies of copper and TPyB adsorption complexes on the $Ti_2CO_2(0001)$

122   surface were determined using spin-unrestricted density functional theory methods as implemented in

123   DMol3 code of Materials Studio software package [64]. The generalized gradient approximation (GGA)

124   with the revised Perdew-Burke-Ernzerhof exchange correlation functional (RPBE) were applied [65]. This

125   functional improves an estimation of the adsorption energy of molecules and atoms on solid surfaces. A

126   double numerical basis set of atomic orbitals including polarization functions for all atoms (DNP) was used

127   [66,67]. The core electrons were replaced by effective core potentials (ECP) [68,69]. The orbital cutoff

128   radius was set to 5.2 Å for all atoms. To consider dispersion effects we used Tkatchenko- Scheffler (TS)

129   method [70–72]. We used the following convergence criteria for geometric optimization: 1.0×10^{-5} Ha for

130   energy, 2.0×10^{-3} Ha/Å for maximum force acting on each atom, and 5.0×10^{-3} Å for maximum displacement

131   of atoms. The tolerance of self-consistent field (SCF) was 1.0×10^{-7}. To accelerate the convergence of SCF

132   calculations we applied the system thermal smearing [73] of 0.005 Ha and algorithm of direct inversion of

133   iterative subspace (DIIS) [74].

134   According to previous experimental and theoretical studies the MXene surfaces are usually

135   terminated by oxygen groups [12,75]. Therefore, as a model of titanium carbide MXene surface we used

136   a rhombic unit cell of Ti_2CO_2 MXene (0001) basal surface with periodic boundary conditions in all cartesian

137   directions. The DFT calculations were carried out in a p(7×7) supercell of Ti_2CO_2(0001) containing 245
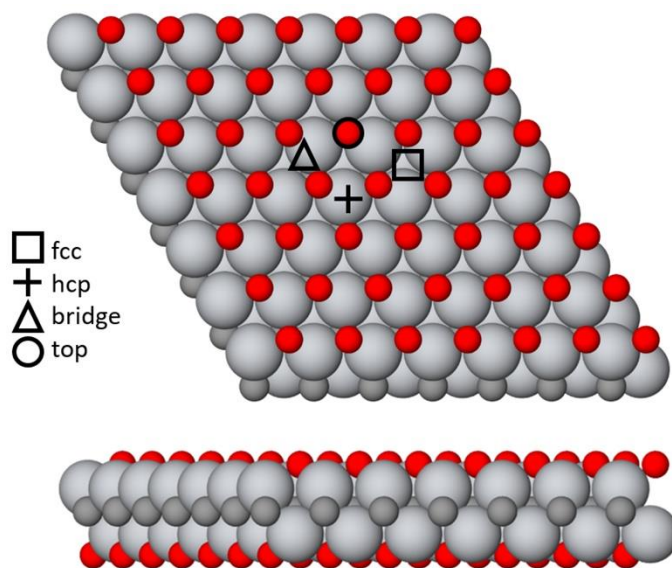
138   atoms (Fig. 1).

139

Fig. 1. Top and side views of the Ti_2CO_2 supercell used in the DFT calculations of the adsorption energies
of Cu and TPyB molecules. Red spheres represent oxygen atoms, gray ones – carbon, light gray – titanium.
Symbols mark the most symmetric O-adsorption sites on the Ti_2CO_2 surface.

143

144   To avoid interaction between supercell replicas in the direction perpendicular to the (0001) surface,

145   the height of the supercell was set to 30 Å, accounting for the vacuum layer of 15.4 Å. The lattice

146   parameter and thickness of the MXene slab after geometric optimization of the supercell including the

147   clean Ti_2CO_2(0001) surface and the vacuum layer were $a = 3.014$ Å and $d = 4.59$ Å, respectively. These

148   values are in good agreement with previously published data [76,77]. We considered the adsorption of a

149   copper atom and TPyB molecule only on the most symmetric O-sites of the Ti_2CO_2(0001) surface: on top,

150   bridge, fcc and hcp sites (Fig. 1). Geometries of all adsorption complexes were optimized with fixed

151   position of all the MXene atoms. The binding energies of the copper atom and TPyB molecule with each

152   adsorption site (E_b) were determined as follows:

$$E_b = E_{a/MX} - (E_a + E_{MX}), \qquad (1)$$

154   where $E_{a/MX}$ is the total energy of the supercell comprising Ti_2CO_2(0001) and TPyB molecule (or Cu atom),

155   E_a is the energy of isolated TPyB molecule (or Cu atom), E_{MX} is the energy of Ti_2CO_2(0001) slab. Table 1

156   shows the DFT calculation results. A more negative value of the binding energy corresponds to a greater

157   stability of the adsorption complex in the ground state of the system.

158

159   **Table 1**

160   Binding energies (in kJ/mol) of the copper atom and TPyB molecule on different adsorption sites of the
161    $Ti_2CO_2(0001)$ surface calculated by the GGA/RPBE method with TS correction. The values in brackets
162   correspond to the fcc2 and hcp2 adsorption complexes of TPyB molecules.

163

	top	bridge	fcc	hcp	Average $\langle E_b^{Cu}\rangle$, $\langle E_b^{TPyB}\rangle$
TPyB	-447	-441	-436(-450)	-451(-441)	-444±6
Cu	-364	-480	-542	-485	-502±34 (bridge, fcc, hcp)

170

171   Structures of the copper adsorption complexes on the $Ti_2CO_2(0001)$ surface are shown in the Fig.S1.

172   The fcc site binds the copper atom most strongly. Difference between the binding energies of the Cu atom

173   with the fcc site and with the hcp, bridge sites are 57 and 62 kJ / mol, respectively. These values do not

174   exceed 12% of the Cu binding energy with the strongest fcc site. The adsorption complexes of copper on

175   the top and bridge sites are metastable, despite the high negative binding energy. They transform into

176   the fcc adsorption complex during the optimization procedure. Copper adsorbed at the hcp site is stable,

177   apparently due to the high diffusion barrier to the fcc site. The binding energy of copper with the top site

178   is -364 kJ/mol, which is 178 kJ/mol (33%) higher than the corresponding value for the fcc site. Thus, the

179    $Ti_2CO_2(0001)$ surface is heterogeneous in terms of the binding energy of copper atoms.

180   Binding the TPyB molecule to the $Ti_2CO_2(0001)$ surface is different. The optimal structures of the

181   TPyB adsorption complexes are shown in Fig. 2. It is clearly seen that dispersion forces dramatically affect

182   the energy and structure of TPyB adsorption complexes. When we turn on the dispersion correction, the

183   adsorbed TPyB molecule became "flat" and distance from its center of mass to the surface decreased from

184   3.9 Å to 2.5 Å. The average binding energy is increased by about 4 times. As it can be seen in Table 1, the

185   binding energy of the molecule is practically independent of its position and orientation in the plane

186   parallel to the surface. The average binding energy is -444 kJ/mol, the absolute deviation does not exceed

187   6 kJ/mol, and the relative deviation is 2%. To verify the weak dependence of the TPyB binding energy on

188 position and orientation of the adsorbed molecule, we have calculated the energy of 12 rotational states

189 of TPyB molecules bound to the top and fcc sites. The rotational states differ from each other by 10°

190 rotation of the TPyB molecule in a plane parallel to the Ti$_2$CO$_2$(0001) surface.
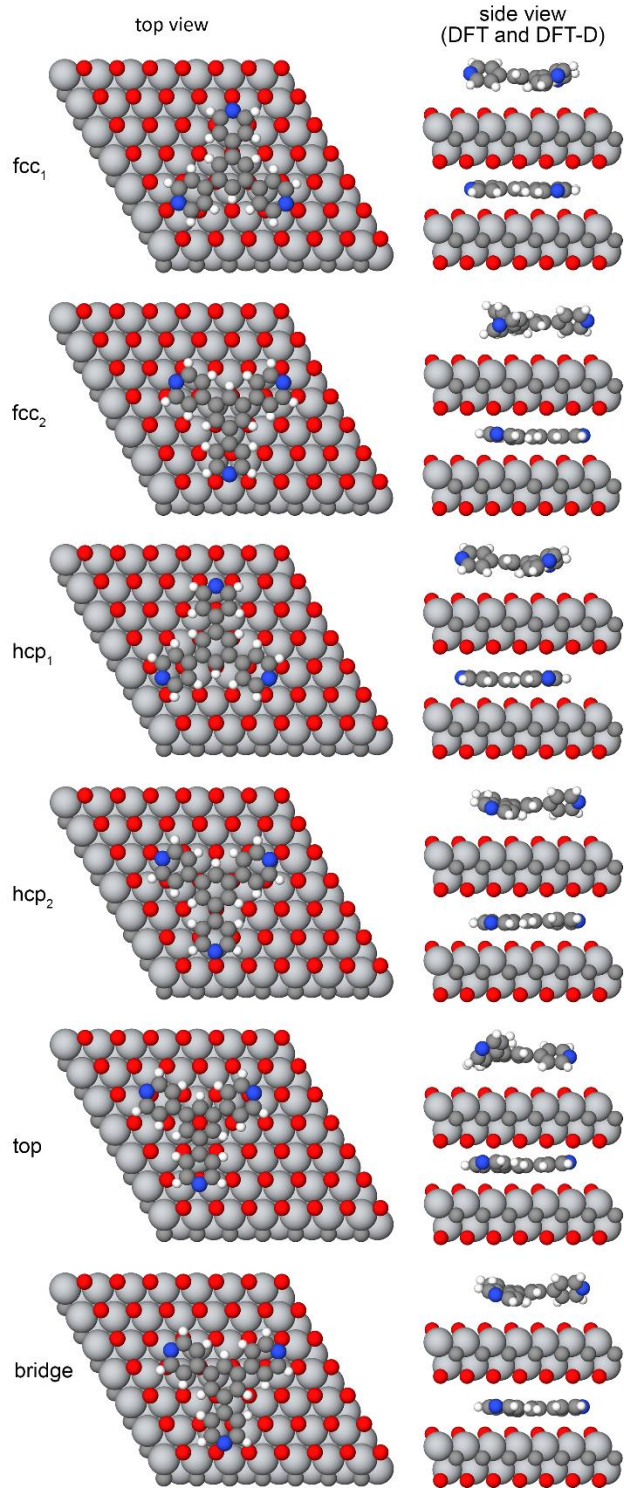
191

192

193 **Fig. 2.** Structures of the TPyB adsorption complexes on the Ti$_2$CO$_2$ surface according to GGA/RPBE
194 calculations. Top side view results from the DFT calculation, bottom side view is DFT+TS result.
195

196   The relative deviation of the binding energy for all the rotational states from the average value also does

197   not exceed 2%. Thus, the Ti$_2$CO$_2$(0001) surface is homogeneous in terms of the TPyB binding energy.

198   Due to the triangular symmetry of the molecule and location of the copper adsorption sites on the

199   Ti$_2$CO$_2$(0001) surface, it can be assumed that metal-organic structures similar to those appearing in the

200   TPyB-Cu layer on the Au (111) surface can also emerge in the TPyB-Cu/Ti$_2$CO$_2$(0001) layer [51–54]. Key

201   elements of all these structures are two-fold Cu(TPyB)$_2$ and three-fold Cu(TPyB)$_3$ coordination motifs with

202   w_d and w_t coordination energies, respectively.

203   To estimate the energies of two-fold w_d and three-fold w_t coordination motifs in the TPyB-

204   Cu/Ti$_2$CO$_2$(0001) layer we had to perform the DFT calculations of the potential energy U of interactions

205   in the unit cells of the honeycomb and triangular phases [51–54] shown in Fig. 3. Developing the atomic

206   models of these phases we relied on the commensurability of their structure with the arrangement of

207   oxygen atoms on the Ti$_2$CO$_2$(0001) surface. The unit cell of the honeycomb structure contains two TPyB

208   molecules and three Cu atoms (Fig. 3a). We have exploited the following feature of this phase. The phase

209   is formed only by two-fold coordination motifs. Unit cell of the honeycomb structure contains 3 two-fold

210   coordination modes. The dense triangular structure consists of identically oriented TPyB molecules, each

211   of them interacts with 3 Cu atoms. The unit cell of the triangular phase (Fig. 3b) consists of one TPyB

212   molecule and one Cu atom forming one three-fold coordination mode. There are no two-fold

213   configurations in this phase. Thus, an estimation of the energies of two-fold and three-fold coordination

214   bonding can be reduced to the geometric optimization of the honeycomb and triangular periodic

215   structures and calculation of the parameters in the following expression (2):

216

217   $$U = E_t - SE_{slab} - N_{TPyB}\left(E_{TPyB} + E_{TPyB}^{ads}\right) - N_{Cu}\left(E_{Cu} + E_{Cu}^{ads}\right), \qquad (2)$$

218   $$E_{TPyB}^{ads} = E_{TPyB/MX} - SE_{slab} - E_{TPyB}, \qquad (3)$$

219   $$E_{Cu}^{ads} = E_{Cu/MX} - SE_{slab} - E_{Cu}. \qquad (3)$$

220

221   E_t is the total energy of the phase unit cell, S is the number of Ti$_2$CO$_2$(0001) slab unit cells in the unit cell

222   of the phase. The unit cells of the honeycomb and triangular phases include 76 and 19 unit cells of the

223 Ti$_2$CO$_2$(0001) slab, respectively. The E_t energies were averaged over 6 different initial positions of the

224 metal-organic layer relative to the Ti$_2$CO$_2$(0001) surface in the case of triangular structure and over 2 initial

225 positions in the case of honeycomb one. The E_{slab} is the energy of clean Ti$_2$CO$_2$(0001) slab unit cell
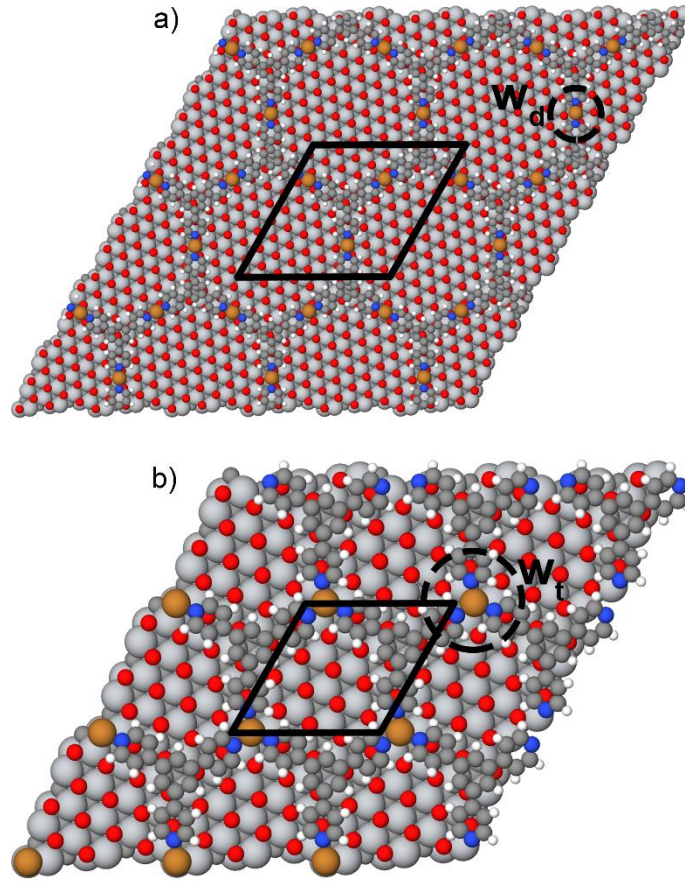
226 obtained by the separate DFT calculation.

227

228 **Fig. 3.** DFT optimized unit cells of honeycomb (a) and triangular (b) phases of TPyB-Cu/Ti$_2$CO$_2$(0001) layer.

229

230 E_{TPyB} and E_{Cu} are the energies of TPyB molecule and copper atom in vacuum. N_{TPyB} and N_{Cu} are the

231 amounts of the TPyB molecules and Cu atoms in the phase unit cell. E_{TPyB}^{ads} and E_{Cu}^{ads} are the binding

232 energy of a single TPyB molecule and a single Cu atom with the Ti$_2$CO$_2$(0001) surface. In the case of E_{Cu}^{ads}

233 we distinguish fcc, hcp and top O-sites of the Ti$_2$CO$_2$(0001) surface. To determine both E_{TPyB}^{ads} and E_{Cu}^{ads}

234 values we have performed separate DFT calculations including geometry optimization procedures for the

235 simulation cells comprising 1 TPyB molecule and 1 Cu atom on 76 and 19 unit cells of the Ti$_2$CO$_2$(0001)

236 slab, correspondingly. $E_{TPyB/MX}$ and $E_{Cu/MX}$ are the total energies of such simulation cells.

237   Since the considered surface-confined metal-organic structures have large unit cells – from 135

238   (triangular phase) to 461 (honeycomb phase) atoms, their optimization was carried out at a lower level of

239   theory. The calculations were performed using SIESTA-4.1.5 code [78] using classical PBE density

240   functional approximation. Due to large size of unit cells only gamma-point calculations were performed.

241   Double-zeta polarized (DZP) basis set was used for all atoms of the adlayer and for upper layers of the

242   MXene including central carbon layer. Lower layers of titanium and oxygen of the MXene were simulated

243   with single-zeta (SZ) basis set. Convergence of Kohn-Sham self-consistent algorithm was checked by

244   Hamiltonian change with tolerance 10^{-4} eV, and by maximum change of the density matrix elements with

245   tolerance 10^{-5} eV. Geometry was relaxed until maximum force acting on each atom was less than 0.005

246   eV/Å.

247   Using this calculation set, we have obtained the following values of the parameters in the

248   expression (2): $E_{slab} = -117850$, $E_{TPyB} = -414873$, $E_{Cu} = -115233$, $E_{TPyB}^{ads} = -334$ and $E_{Cu}^{ads} =$

249   -177 in kJ/mol. In the case of E_{Cu}^{ads} we virtually have -199, -186, -146 kJ/mol for fcc, hcp and top O-sites,

250   respectively. The $E_{Cu}^{ads} = -177$ kJ/mol is the average value. Total energies E_t of the honeycomb and

251   triangular phases unit cells shown in the Fig. 3 are -2769894 ± 12 and -10133926 ± 3 kJ/mol.

252   As it clearly seen in the Fig.4, $U_{HON} = 3w_d$ for the honeycomb structure, and $U_{TR} = w_t$ for the

253   triangular phase. Therefore, the following energies of two-fold and three-fold TPyB-Cu coordination

254   bonding on the Ti$_2$CO$_2$(0001) surface can be easily derived $w_d = 206$ kJ/mol and $w_t = 104$ kJ/mol.

255   To evaluate the effect of dispersion forces on the energies of two-fold Cu(TPyB)$_2$ and three-fold

256   Cu(TPyB)$_3$ coordination modes determined from the DFT calculations of the unit cells of the honeycomb

257   and triangular structures, we have performed extra DFT calculations taking into account the DFT-D4

258   correction [79,80]. The energies of two-fold and three-fold coordination modes change as follows: -199

259   kJ/mol with D4 correction versus -206 kJ/mol without correction for Cu(TPyB)$_2$ and -88 kJ/mol with D4

260   correction versus -104 kJ/mol without it for Cu(TPyB)$_3$. The energy of Py-Cu coordination interaction

261   related to these values changes by 3.5 kJ/mol from -102.8 kJ/mol to -99.3 kJ/mol. This value is comparable

262   to the thermal energy at 400K. Such insignificant contribution of dispersion interactions to the potential

263   energy of the considered metal-organic layer can be explained by the local character of the short-ranged

264   Cu-N coordination bonding, which are the strongest interaction in the system. In the lattice model of TPyB-

265   Cu layer on the Ti₂CO₂(0001) surface we will use original values of w_d and w_t parameters calculated

266   without dispersion correction.

267   At the obtained energies of two-fold Cu(TPyB)₂ and three-fold Cu(TPyB)₃ coordination bonding the

268   w_t/w_d ratio is considerably less than 1. This calls into question the emergence of the flower-like TPyB-Cu

269   phases on the Ti₂CO₂(0001) surface despite they are observed on the Au (111) surface [54]. In this case,

270   the two-fold coordination bonding is significantly stronger than three-fold one. A series of flower-like

271   phases is formed when $w_t/w_d > 1$. Therefore, the self-assembly of ordered metal-organic structures in

272   the considered adsorption monolayer commensurable with Ti₂CO₂(0001) surface is doubtful. It requires

273   further research with statistical methods.

274

275   **3. Lattice model of TPyB-Cu/Ti₂CO₂(0001) layer**

276   A lattice model of surface-confined metal-organic structures assumes by definition their

277   commensurability with an atomic structure of the surface. In our case, the TPyB-Cu structures are assume

278   to be commensurable with the arrangement of oxygen atoms on the Ti₂CO₂(0001) surface. Thus, we

279   consider the adsorption of a copper atom and TPyB molecule only on the most symmetric O-sites of the

280   surface: on top, bridge, fcc and hcp sites. In addition, a correct model of TPyB-Cu self-assembly should

281   account for the energetic heterogeneity of the Ti₂CO₂(0001) surface with respect to the adsorption of

282   copper atoms. To simplify the model, we consider only the largest difference (28% or 138 kJ/mol) in the

283   binding energy of Cu with the "weak" top site compared to the average binding energy with the "strong"

284   sites (fcc, hcp, and bridge). Let us take this difference into account with a parameter $\Delta = E_b(top) -$

285    $\langle E_b^{Cu} \rangle = 138$ kJ/mol, where $E_b(top)$ is the binding energy of Cu with the top site, and $\langle E_b^{Cu} \rangle$ is the

286   average binding energy of Cu with fcc, hcp and bridge sites. This assumption allows us to treat qualitatively

287   the surface heterogeneity effects.

288   As the surface model we have chosen a heterogeneous triangular lattice with parameter $a = r/\sqrt{3}$,

289   where r is the distance between neighboring oxygen atoms on the Ti₂CO₂(0001) surface (Fig. 4). Such

290   triangular lattice is formed by three types of nodes corresponding to the fcc, hcp and top sites on the

291   Ti$_2$CO$_2$(0001) surface. As one can see, the bridge sites are not considered in the model. This simplification

292   is supposed to have no qualitative effects on the phase behavior of the considered adsorption layer.

293   Indeed, the deviation of the copper binding energy with the bridge site from the average binding energy
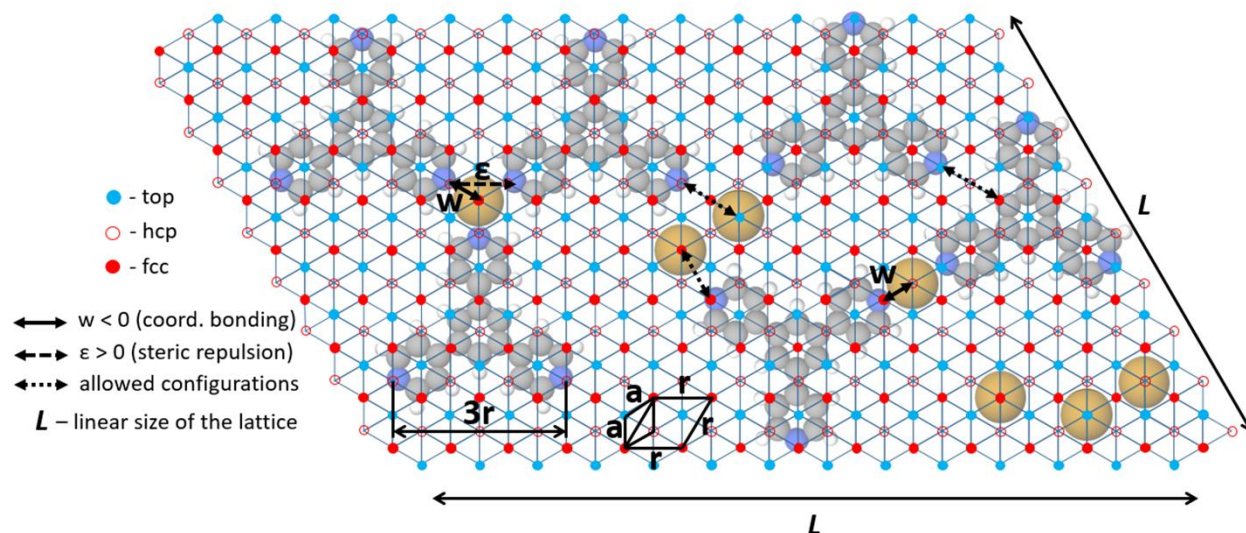
294   on the "strong" sites is less than 4.5%.

295

296   **Fig. 4.** Lattice model of adsorption of TPyB molecules and Cu atoms on the top, fcc and hcp sites of the
297   Ti$_2$CO$_2$(0001) surface. Top, fcc and hcp sites form the heterogeneous triangular lattice. The arrows indicate
298   pair interactions included in the model.

299

300   The adsorbed copper atom occupies one lattice site in all the cases. When an isolated copper atom is

301   adsorbed on the "strong" sites, the total energy of the system changes be the value $\langle E_b^{Cu} \rangle - \mu_{Cu}$, where

302   $\langle E_b^{Cu} \rangle$ is the average binding energy of Cu with "strong" sites, μ_{Cu} is the chemical potential of copper

303   related to its partial pressure in the gas phase equilibrated with the adsorption layer. When a copper atom

304   is adsorbed on the "weak" top site, the Δ value is additionally included in the total energy of the system,

305   thus it changes by the value $\langle E_b^{Cu} \rangle - \mu_{Cu} + \Delta$.

306   As shown in Fig. 4, the adsorbed TPyB molecule occupies several sits of the triangular lattice with

307   the parameter $a = r/\sqrt{3}$. In this model the distance between nitrogen atoms of the pyridine rings of the

308   adsorbed TPyB molecule is $3r$. Thus, the model also considers the relative size of the linker molecule. To

309   develop lattice models of experimentally observed TPyB-Cu metal-organic structures [51–54], it is

310   necessary to take into account at least two possible orientations of the TPyB molecule, which differ in

311   rotation by 60 ° in the plane parallel to the surface. In the proposed model, these states correspond to

312   the molecules with pyridine ring down and up. Recall the Ti$_2$CO$_2$(0001) surface is homogeneous in terms

313   of the TPyB binding energy. In this case, the additional parameters are not required. When an isolated

314   TPyB molecule is adsorbed, the total energy of the system changes by the value $\langle E_b^{TPyB} \rangle - \mu_{TPyB}$

315   regardless of the adsorption site and in-plane orientation of the molecule. Here, $\langle E_b^{TPyB} \rangle$ is the average

316   binding energy of the molecule with the Ti$_2$CO$_2$(0001) surface, and μ_{TPyB} is the TPyB chemical potential

317   associated with the partial pressure of TPyB in the equilibrium gas phase. Thus, our model includes 9

318   adsorption complexes. These are 3 adsorption complexes of copper on the top, hcp, and fcc sites. There

319   are also 6 adsorption complexes of the TPyB molecule corresponding to the same sites. The adsorbed

320   molecule has two possible orientations on each site – "up" and "down".

321   We considered the interactions in all different pairs of adsorption complexes, where the centers of

322   the adsorbates are located at the distance less than 18 Å. There were 631 such pair configurations. Among

323   them 219 pair configurations, where the distance between nearest atoms belonging to different

324   adsorption complexes is less than the sum of their van der Waals radii. To preserve the simplicity of the

325   model, the adsorbates in the latter cases were assumed to overlap and the interaction potential was

326   considered formally infinite. The van der Waals radii of atoms were determined according to S. Alvarez et

327   al [81]. The exceptions were specific pair configurations with interaction energies w and ε related to the

328   coordination bonding and shown in Fig. 4. These configurations are necessary for the formation of two-

329   fold Cu(TPyB)$_2$ and three-fold Cu(TPyB)$_3$ coordination motifs (Fig. 3 and Fig. 4). Since $w_d = 2w$, and $w_t =$

330    $3w + 3\varepsilon$ (by definition), we had easily derived the w energy of coordination bond and the ε energy of

331   steric repulsion between pyridine rings in the three-fold coordination junction from our DFT calculations

332   data. At given values of $w_d = 206$ kJ/mol and $w_t = 104$ kJ/mol parameters we obtain $w = -102.8$

333   kJ/mol and $\varepsilon = 68.1$ kJ/mol. In addition, the neighboring of two TPyB molecules with the same orientation

334   at the distance of $6a$ between their centers is also allowed. Such pair configuration emerges as the result

335   of compression of the TPyB-Cu layer, for example, on the Au(111) surface [52]. The TPyB-Cu interaction

336   energies in two paired configurations close to the coordination bonding but characterized by a large TPyB-

337   Cu distance (Fig. 4) were set equal to zero, even though the van der Waals radii N atom of the pyridine

338   ring and copper atom overlap in these configurations. It was done to facilitate the pseudo-dynamics of

339   the metal-organic network formation in the Monte Carlo simulations.

340   Key interactions guiding the self-assembly of metal-organic structures are coordination bonds. For

341   this reason, the interaction energies in the remaining 412 configurations characterized by relatively large

342   distances between the adsorbates were set equal to zero to avoid complicating the model. The above-

343   mentioned energies of all the pair interactions are explicitly included in the model and make the

344   corresponding contribution to the total energy of the layer. All specific paired configurations are listed in

345   the Supplementary Material (Fig. S1).

346   The described lattice model, which includes the set of all adsorption complexes and paired

347   configurations, can be downloaded from the SuSMoST website or from the project page at gitlab.com

348   [82,83].

349

350   **4. Details of Monte Carlo simulation**

351   The lattice model of TPyB-Cu layer on Ti$_2$CO$_2$(0001) surface was studied with grand canonical Monte

352   Carlo (GCMC) simulation. The values of $\langle E_b^{Cu} \rangle$, $\langle E_b^{TPyB} \rangle$, Δ, w, ε parameters given in the Section 3 were

353   constant during the simulation. Thus, density, composition, and structure of the model metal-organic

354   layer can be regulated only by temperature and chemical potentials of the components – μ_{TPyB} and μ_{Cu}.

355   Recall the chemical potentials are related to the partial pressures and vapor pressures of these

356   components in the equilibrium gas phase and can be calculated using a suitable equation of state. Partial

357   pressures of the components are related to their mole fractions and total pressure in the gas phase. Since

358   the vapor pressures of TPyB and Cu are very low (ultra-high vacuum conditions), we suppose the most

359   appropriate way to control the partial pressure or chemical potential of the components is to change the

360   molar composition of the gas phase.

361   The GCMC simulations were performed using the SuSMoST 1.1 code [84]. The simulations were

362   performed using the heterogeneous triangular lattice of $L \times L$ centers with periodic boundary conditions

363   (Fig. 4). The linear size of the lattice $L = 144$ was chosen large enough to avoid the influence of the finite

364   size of the system on the calculated values. It also took into account the periodicity of the metal-organic

365   structures formed during the simulation. Each Monte Carlo simulation step includes $L \times L$ attempts to

366   change the state of the adsorption layer through adsorption/desorption, surface diffusion of TPyB

367   molecules and Cu atoms, or in-plane rotation of TPyB molecules. The acceptance probability of a new

368   configuration of the model metal-organic layer was determined by the standard Metropolis algorithm

369   [85]. If the total energy $\mathcal{H}$ of a new state of the system is less than the energy of the previous state

370      $(\Delta\mathcal{H} \leq 0)$, then the change in the system state was accepted. Otherwise $(\Delta\mathcal{H} > 0)$, the new state of the

371   adsorption layer was accepted with the probability $\min\{1, \exp(\Delta\mathcal{H}/RT)\}$.

372   The total energy of the adsorption layer includes the contributions of all the interactions and fields

373   expressed in terms of the following model parameters $\langle E_b^{Cu}\rangle$, $\langle E_b^{TPyB}\rangle$, Δ, w, ε, μ_{TPyB} and μ_{Cu}. We used

374   10^6 Monte Carlo steps to reach the equilibrium state and calculate ensemble averages. Thereby we have

375   calculated the total and partial densities $\rho = (\langle N_{\mathrm{TPyB}}\rangle + \langle N_{\mathrm{Cu}}\rangle)/L^2$, $\rho_{\mathrm{TPyB}} = \langle N_{\mathrm{TPyB}}\rangle/L^2$, $\rho_{\mathrm{Cu}} =$

376      $\langle N_{\mathrm{Cu}}\rangle/L^2$, potential energy $\langle U\rangle = \langle\mathcal{H}\rangle - \mu_{TPyB}\langle N_{\mathrm{TPyB}}\rangle - \mu_{Cu}\langle N_{\mathrm{Cu}}\rangle$ and heat capacity $C_\mu =$

377      $L^2\left(\langle U^2\rangle - \langle U\rangle^2\right)/RT^2$ of the adsorption layer. The parallel tempering algorithm [86] was used to improve

378   the convergence to the equilibrium state and calculate temperature dependences of the adlayer

379   characteristics.

380

381   **5. Results and Discussion**

382   *5.1 Ground state of the TPyB-Cu/Ti₂CO₂(0001) model*

383   It is convenient to begin an analysis of the model phase behavior by calculating the $\left(\mu_{\mathrm{TPyB}}, \mu_{\mathrm{Cu}}\right)$-

384   regions of existence for different phases at absolute zero, using the principle of a minimum grand

385   thermodynamic potential $\Omega\left(\mu_{\mathrm{TPyB}}, \mu_{\mathrm{Cu}}, \langle E_b^{Cu}\rangle, \langle E_b^{TPyB}\rangle, \Delta, w, \varepsilon\right)$ in equilibrium state of the open system.

386   In this case, the entropy contribution to the free energy of the system is not considered. For given values

387   of μ_{TPyB} and μ_{Cu}, a phase with the minimum Ω value is stable.

388   This approach assumes lattice models of all the structures under consideration available as well as

389   the corresponding $\Omega\left(\mu_{\mathrm{TPyB}}, \mu_{\mathrm{Cu}}, \langle E_b^{Cu}\rangle, \langle E_b^{TPyB}\rangle, \Delta, w, \varepsilon\right)$ expressions for each of them. We have

390   developed the lattice models of well-known "flower" phases (Fig. S2, Supplementary Material), assuming

391   the phase behavior of the TPyB-Cu layer on Ti₂CO₂(0001) similar to that on Au(111) surface [51–54].

392   However, the w_t/w_d ratio is significantly less than unity in the developed model. It indicates the low

393   probability of three-fold coordination motif (TPyB)₃Cu to emerge in the adlayer. Preliminary GCMC

394   simulation have confirmed this assumption. Therefore, in addition to the "flower" phases, we have

395   developed lattice models of metal-organic structures formed exclusively by one- and two-fold

396   coordination motifs (Fig. S2, Supplementary Material). We have derived the expression for the grand

397   thermodynamic potential per one lattice site for each metal-organic structure (Supplementary Material).

398   Applying the described method, we have calculated the ground state $(\mu_{\text{TPyB}}/|w|, \mu_{\text{Cu}}/|w|)$-phase

399   diagram of the TPyB-Cu adsorption layer on Ti₂CO₂(0001) surface (Fig. 5).

400

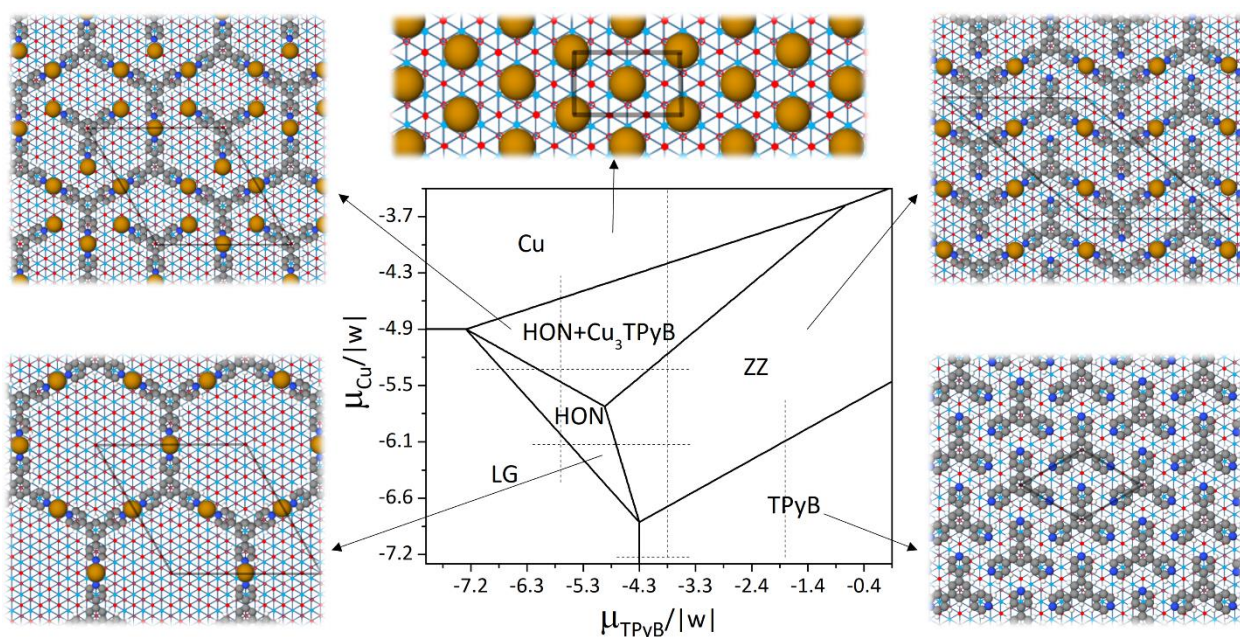**Fig. 5.** Phase diagram of the TPyB-Cu layer on Ti₂CO₂(0001) surface in $(\mu_{\text{TPyB}}/|w|, \mu_{\text{Cu}}/|w|)$-coordinates.
The GCMC simulations were performed along the dotted lines.

403

404   As we can see in the Fig. 5, only the honeycomb structure (HON) is formed at large negative values

405   of the TPyB chemical potential corresponding to a low relative pressure. A hexagon side in the HON

406   structure consists of two TPyB molecules coordinated by one Cu atom. Due to the assumed

407   commensurability of the HON structure with the lattice of oxygen atoms of the Ti₂CO₂(0001) surface, all

408   Cu atoms of this metal-organic structure are located at the same sites – fcc or hcp. Top O-sites of the

409   Ti₂CO₂(0001) surface remain unoccupied because of the energetic penalty Δ. It is also true for the other

410   surface-confined TPyB-Cu structures. Increase of the Cu partial pressure (chemical potential) initially

411   induces filling of the two-dimensional pores of the HON structure with Cu_3TPyB complexes, and further

412   the surface is covered by the copper. Increasing TPyB partial pressure over the HON structure causes its

413   transformation into the zigzag metal-organic phase (ZZ). TPyB molecules in the ZZ structure are linked by

414   Cu atoms into one-dimensional zigzag chains. Thus, each Cu atom in the ZZ structure coordinates two

415   TPyB molecules. A further growth of the TPyB partial pressure over the ZZ phase promotes the formation

416   of a pure organic phase.

417   Fig. 5 shows that organic TPyB layer on $Ti_2CO_2(0001)$ surface can be used as a precursor for a

418   synthesis of the TPyB-Cu metal-organic structures. In this case, an increase of the Cu partial pressure will

419   first lead to the ZZ phase, and then either to the HON structure filled with Cu_3TPyB complexes, or to the

420   pure metallic phase depending on the fixed partial pressure of TPyB.

421

422   *5.2 Results of the Monte Carlo simulation at nonzero temperatures*

423   Here we present our results on the GCMC simulation of the TPyB-Cu layer at nonzero temperatures.

424   These simulations are aimed to verify the structure of the ground state phase diagram and to evaluate

425   temperature effects. In Fig. 6 illustrates the dependences of the adsorption layer density on the chemical

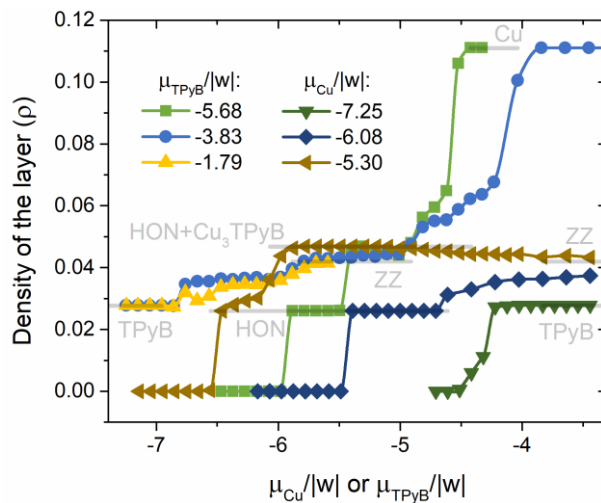426   potential of Cu or TPyB at the constant temperature $RT/|w| = 0.024$.

427

428   **Fig. 6.** Density (ρ) of the adsorption layer vs. chemical potentials $\mu_{TPyB}/|w|$ and $\mu_{Cu}/|w|$ of the
429   components at $RT/|w| = 0.024$. Three adsorption isotherms have been calculated by increasing the Cu
430   chemical potential $\mu_{Cu}/|w|$ at the constant values of $\mu_{TPyB}/|w|$: -5.68, -3.83 and -1.79. The dependences
431   of the adlayer density on the TPyB chemical potential $\mu_{TPyB}/|w|$ have been obtained at the constant
432   values of $\mu_{Cu}/|w|$: -7.25, -6.08, -5.30. Density levels of the ideal HON, HON+Cu_3TPyB, ZZ, TPyB and Cu
433   structures are shown in light grey.

434

435 Such curves will be further referred to as adsorption isotherms. The adsorption isotherms were calculated

436 along the corresponding vertical and horizontal lines on the ground state phase diagram of the system

437 (Fig. 5).

438 There are horizontal plateaus on the calculated adsorption isotherms. These plateaus reveal the

439 formation of organic, metal-organic, and metallic structures in the adlayer, which are resistant to changes

440 in external pressure of components. Density levels of the ideal structures are shown in light grey in the

441 Fig. 6. As it follows from the Fig. 6, the TPyB-Cu metal-organic structures on the Ti_2CO_2 surface can be

442 obtained in two ways.

443 The first approach is a condensation of the surface gas into the HON structure (Fig. 7a) by increasing

444 partial pressures of the components in the equilibrium gas phase. This process is pronounced in the

445 adsorption isotherms as the abrupt change of the adlayer density from zero to 0.026 TPyB molecules and

446 Cu atoms per one lattice site. Depending on the fixed value of the Cu chemical potential, an increase in

447 the TPyB chemical potential over the HON structure either leads to emergence of the HON+Cu_3TPyB phase

448 (Fig.8b) and the ZZ phase further (Fig.8c), or the ZZ phase appears at once, bypassing the HON+Cu_3TPyB

449 structure. At very low partial pressures of copper, for example $\mu_{Cu}/|w| = -5.30$, an increase in the TPyB

450 partial pressure above the surface gas results in the formation of a pure organic phase TPyB (Fig. 7d). The

451 HON structure can be also condensed from the surface gas phase by increasing partial pressure of copper

452 at a fixed TPyB pressure, for example at $\mu_{TPyB}/|w| = -5.68$. A growth of the Cu partial pressure over the

453 HON structure initiates the filling of its 2D pores with Cu_3TPyB complexes. Thus, the HON+Cu_3TPyB phase

454 emerges. A further growth of the Cu partial pressure leads to a gradual covering of the surface with copper

455 islands and desorption of TPyB molecules (Fig. 7e). Ultimately, all adsorption O-sites of the Ti_2CO_2 surface

456 are covered with copper (Fig. 7f). TPyB-Cu metal-organic structures on $Ti_2CO_2(0001)$ surface can also be

457 synthesized by increasing partial pressure of copper over the pure organic TPyB phase. In this case, we

458 observe nucleation and growth of islands with a zigzag ZZ structure (Fig. 7g). If the fixed $\mu_{TPyB}/|w|$ is close

459 to the values at which the pure organic phase condenses on the Ti_2CO_2 surface, a further increase in the

460 Cu partial pressure changes the topology of metal-organic layer. The one-dimensional ZZ structure

461   gradually transforms to the two-dimensional HON+Cu₃TPyB phase (Fig. 7h). It is worth to note the

462   dynamic feature of HON+Cu₃TPyB phase, in which the Cu₃TPyB complexes inside the 2D pores of the

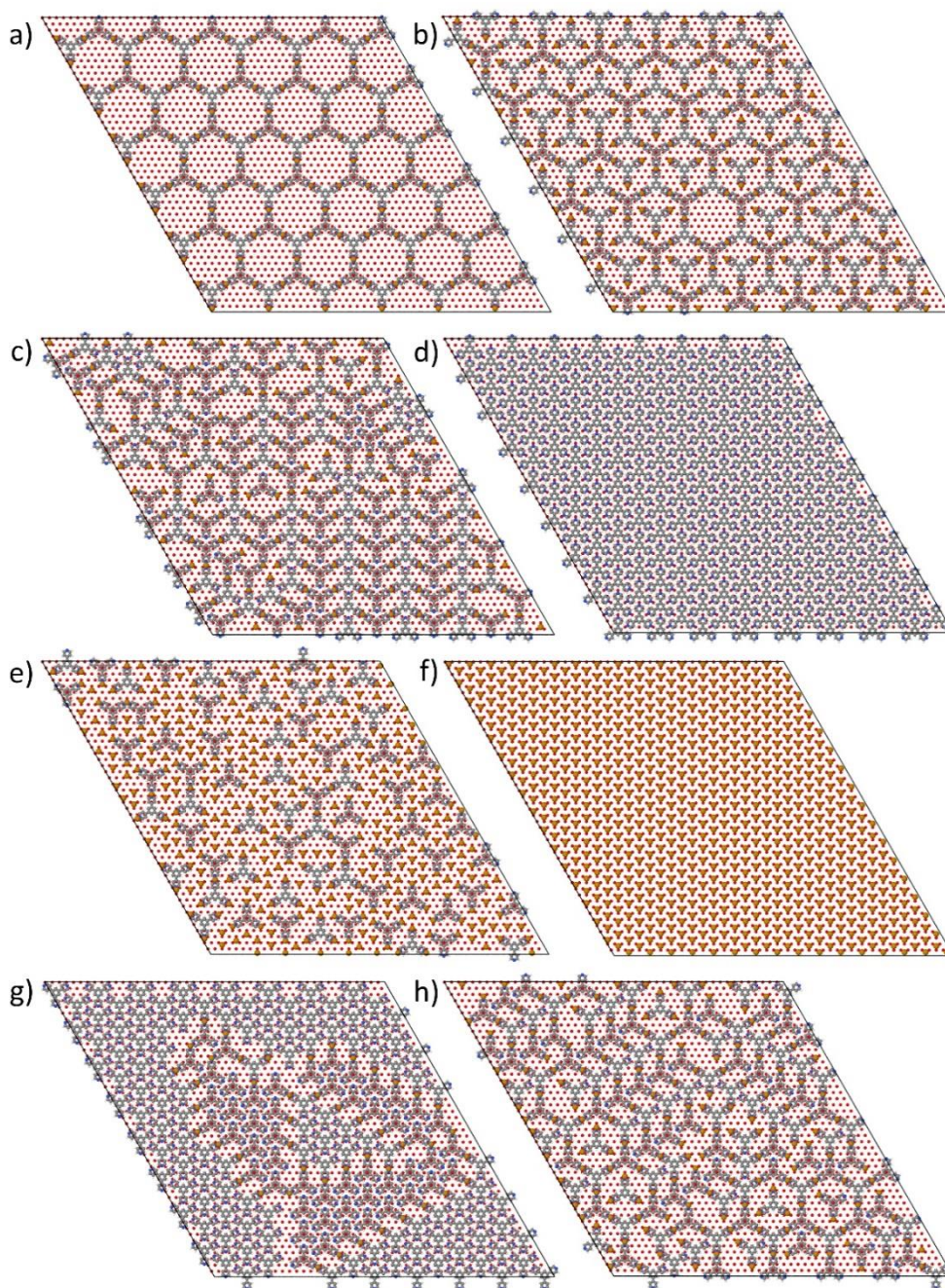463   hexagons have translational and rotational mobility.

464

Fig. 7. Snapshots of the model adsorption layer of TPyB-Cu on $Ti_2CO_2(0001)$ obtained in the GCMC simulation at $RT/|w| = 0.024$ and the following chemical potentials $\left(\mu_{TPyB}/|w|, \mu_{Cu}/|w|\right)$: a) HON phase (-5.68, -5.69); b) HON+Cu₃TPyB phase (-5.88, -5.30); c) ZZ phase (-3.83, -5.79); d) TPyB phase (-3.83, -7.06); e) transition from HON+Cu₃TPyB phase to Cu phase (-5.68, -4.62); f) Cu phase (-5.68, -4.43); g) transition from TPyB phase to ZZ phase (-1.79, -6.57); h) transformation of the HON+Cu₃TPyB phase to ZZ phase (-3.83, -5.40).

473   Apparently, it reduces the free energy of HON+Cu$_3$TPyB structure making its formation at low partial

474   pressures of TPyB more favorable than the ZZ structure. The subsequent growth of the Cu chemical

475   potential leads to the filling of the surface with copper (Fig. 7e, f).
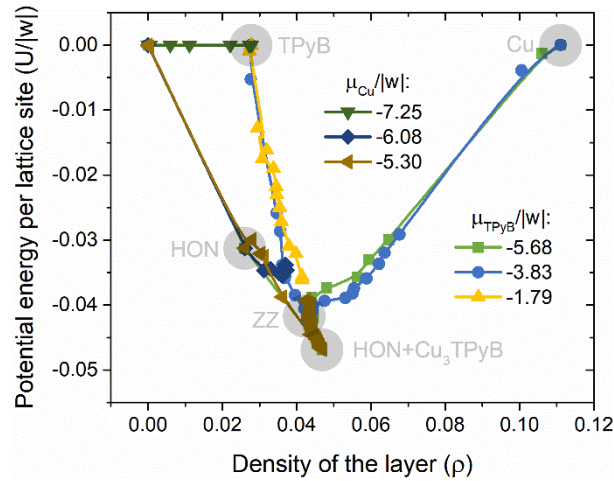
476

477

Fig. 8. Potential energy of the TPyB-Cu layer per lattice site vs. layer density (ρ) at $RT/|w| = 0.024$. The symbols are results of the GCMC simulations with the fixed chemical potential of one component and varying another (see the values in the legend). Light grey circles mark out the $(U/|w|, \rho)$ -regions corresponding to the ideal HON, HON+Cu$_3$TPyB, ZZ, TPyB and Cu phases.

482

483   Fig. 8 illustrates how the potential energy of TPyB-Cu/Ti$_2$CO$_2$ layer changes with its density. Light

484   gray circles mark out the $(U/|w|, \rho)$ -regions corresponding to the ideal HON, HON+Cu$_3$TPyB, ZZ, TPyB

485   and Cu phases. The crowding of GCMC points in these regions unambiguously confirms the existence of

486   the above-described metal-organic structures with the inherent densities and potential energies. These

487   curves can also be used to estimate the transitions from one phase to another induced by varying the

488   chemical potentials of the components. As it follows from the Fig.9, the transitions from the surface gas

489   to the TPyB phase, from the TPyB phase to the ZZ structure, and from the ZZ structure to HON+Cu$_3$TPyB

490   phase are continuous. Whereas the HON structure from the surface gas and the Cu phase from the metal-

491   organic phases occur abruptly.

492   Thus, copper single atoms can be stabilized on the Ti$_2$CO$_2$ surface in three different metal-organic

493   structures. Each copper atom in the HON and ZZ structures coordinates two pyridine rings of neighboring

494   TPyB molecules. Local environments of the Cu atoms in these structures are different. In the case of

495   HON+Cu$_3$TPyB structure, there are both one- and two-fold coordination motifs. Hexagonal pores of this

496 structure formed by TPyB-Cu-TPyB bonding are occupied by Cu$_3$TPyB complexes, where each Cu atom is

497 bonded to a single pyridine group. The local environment of the Cu atoms included in the surface-confined

498 metal-organic networks obviously affect the electronic structure of the Cu sites. We suggest this to use in

499 the development of ORR/OER catalysts. We have estimated relative thermal stabilities of the found metal-

500 organic structures. Fig. 9 demonstrates temperature dependences of the heat capacities calculated for

501 the HON, HON+Cu$_3$TPyB, and ZZ phases at fixed values of the chemical potentials of both components.

502 Corresponding adsorption isobars (dependence of the adlayer density on temperature) are shown in the

503 inset to the Fig. 9. Positions of the heat capacity peaks and inflections/steps on the adsorption isobars for

504 a given phase indicate its destruction temperature. The heat capacities and isobars were calculated at

505 different sets of the chemical potentials for each phase (see Fig. S3, Supplementary Material). Only the

506 most thermally stable states defined by the $\left(\mu_{\text{TPyB}}/|w|, \mu_{\text{Cu}}/|w|\right)$-set are shown in the Fig. 9. As one can

507 see, the most stable phase is ZZ. The destruction temperature of ZZ phase is more than two times higher

508 the destruction temperature of the HON and HON+Cu$_3$TPyB phases. The destruction temperature of the

509 HON+Cu$_3$TPyB structure is slightly higher than that of the HON structure. Thus, filling the 2D pores of the

510 HON structure with Cu$_3$TPyB complexes stabilizes the adsorption layer. The Cu$_3$TPyB complexes in the 2D

511 pores can affect thermal stability of the metal-organic layer in two possible ways.
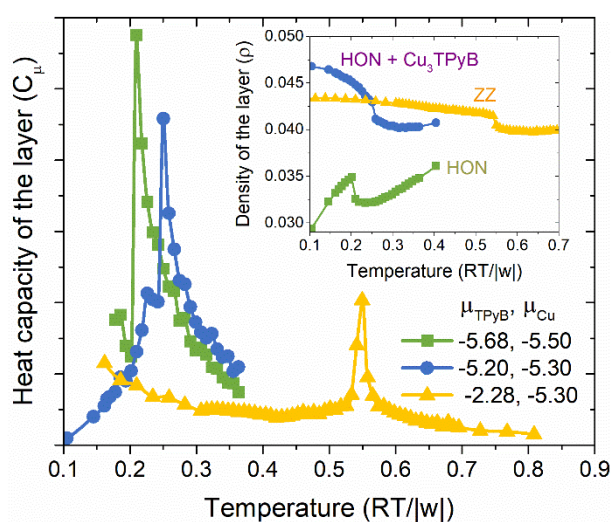
512

513

514 **Fig. 9.** Heat capacity and density (on the inset) of the HON, HON+Cu$_3$TPyB and ZZ phases in TPyB-Cu
515 adsorption layer vs. $RT/|w|$ at the constant chemical potentials (partial pressures) of both components
516 $\mu_{\text{TPyB}}/|w|$ and $\mu_{\text{Cu}}/|w|$.

517

518   On the one hand, this raises the entropy impact to the free energy of the structure due to the translational

519   and rotational mobility of Cu_3TPyB complexes inside the pores. On the other hand, this prohibits a jump

520   of the molecule into the pore due to thermal fluctuations.

521

522   **6. Conclusion**

523   In this work, we have estimated the possibility of stabilizing copper single atoms on the oxygen-

524   terminated titanium carbide surface through the self-assembly of surface-confined metal-organic

525   structures comprising 1,3,5-tris(pyridyl)benzene. Can such metal-organic structures self-assemble on the

526   MXene surfaces? The question is of fundamental importance. The positive answer opens up the possibility

527   of "tuning" the catalytic properties of such systems, for example in ORR/OER reactions.

528   Based on the DFT calculations of the geometries and energies of key adsorption complexes and

529   structures, we developed the lattice model of the TPyB-Cu adsorption layer on $Ti_2CO_2(0001)$ surface. The

530   ground state analysis of the model and grand canonical Monte Carlo simulations at nonzero temperatures

531   allow us to draw the following conclusions:

532   1) The oxygen-terminated titanium carbide surface is energetically heterogeneous with respect to

533   the adsorption of copper and homogeneous (with "chemical" accuracy) in terms of the TPyB adsorption.

534   2) Due to steric hindrances arising during in the three-fold $Cu(TPyB)_3$ coordination motifs, metal-

535   organic structures consisting of two-fold $Cu(TPyB)_2$ coordination modes predominantly appear on the

536    $Ti_2CO_2(0001)$ surface. These are honeycomb (HON), filled-honeycomb (HON+Cu_3TPyB), and zigzag (ZZ)

537   phases. Thus, copper single atoms on the Ti_2CO_2 surface those catalytically active in the ORR reaction can

538   be stabilized in the surface-confined metal-organic structures. These structures differ in the coordination

539   number of copper atoms and their local environment.

540   3) Thermal stability of metal-organic structures in TPyB-Cu/$Ti_2CO_2(0001)$ layer decreases in the

541   following series: zigzag, filled-honeycomb, honeycomb.

542   Analysis of the catalytic activity descriptors for the found metal-organic structures and their stability

543   under ORR/OER conditions is the subject of our future studies. We hope that our results will stimulate

544   further experimental studies of hybrid "metal-organic network/MXene" catalysts.

545

549

References

[1] A. Morozan, B. Jousselme, S. Palacin, Low-platinum and platinum-free catalysts for the oxygen reduction reaction at fuel cell cathodes, Energy Environ. Sci. 4 (2011) 1238–1254. https://doi.org/10.1039/C0EE00601G.

[2] J. Suntivich, H.A. Gasteiger, N. Yabuuchi, H. Nakanishi, J.B. Goodenough, Y. Shao-Horn, Design principles for oxygen-reduction activity on perovskite oxide catalysts for fuel cells and metal–air batteries, Nat. Chem. 3 (2011) 546–550. https://doi.org/10.1038/nchem.1069.

[3] M.K. Debe, Electrocatalyst approaches and challenges for automotive fuel cells, Nature. 486 (2012) 43–51. https://doi.org/10.1038/nature11115.

[4] Y. Chen, S. Ji, S. Zhao, W. Chen, J. Dong, W.-C. Cheong, R. Shen, X. Wen, L. Zheng, A.I. Rykov, S. Cai, H. Tang, Z. Zhuang, C. Chen, Q. Peng, D. Wang, Y. Li, Enhanced oxygen reduction with single-atomic-site iron catalysts for a zinc-air battery and hydrogen-air fuel cell, Nat. Commun. 9 (2018) 5422. https://doi.org/10.1038/s41467-018-07850-2.

[5] Q. Peng, J. Zhou, J. Chen, T. Zhang, Z. Sun, Cu single atoms on Ti2CO2 as a highly efficient oxygen reduction catalyst in a proton exchange membrane fuel cell, J. Mater. Chem. A. 7 (2019) 26062–26070. https://doi.org/10.1039/C9TA08297B.

[6] L. Yang, J. Shui, L. Du, Y. Shao, J. Liu, L. Dai, Z. Hu, Carbon-Based Metal-Free ORR Electrocatalysts for Fuel Cells: Past, Present, and Future, Adv. Mater. 31 (2019) 1804799. https://doi.org/10.1002/adma.201804799.

[7] D.-W. Wang, D. Su, Heterogeneous nanocarbon materials for oxygen reduction reaction, Energy Environ. Sci. 7 (2014) 576–591. https://doi.org/10.1039/C3EE43463J.

[8] Z.W. Seh, J. Kibsgaard, C.F. Dickens, I. Chorkendorff, J.K. Nørskov, T.F. Jaramillo, Combining theory and experiment in electrocatalysis: Insights into materials design, Science. 355 (2017) eaad4998. https://doi.org/10.1126/science.aad4998.

[9] J. Zhang, H. Yang, B. Liu, Coordination Engineering of Single-Atom Catalysts for the Oxygen Reduction Reaction: A Review, Adv. Energy Mater. 11 (2021) 2002473. https://doi.org/10.1002/aenm.202002473.

[10] X. Wang, Z. Li, Y. Qu, T. Yuan, W. Wang, Y. Wu, Y. Li, Review of Metal Catalysts for Oxygen Reduction Reaction: From Nanoscale Engineering to Atomic Design, Chem. 5 (2019) 1486–1511. https://doi.org/10.1016/j.chempr.2019.03.002.

[11] B. Qiao, A. Wang, X. Yang, L.F. Allard, Z. Jiang, Y. Cui, J. Liu, J. Li, T. Zhang, Single-atom catalysis of CO oxidation using Pt1/FeOx, Nat. Chem. 3 (2011) 634–641. https://doi.org/10.1038/nchem.1095.

[12] J. Zhang, Y. Zhao, X. Guo, C. Chen, C.-L. Dong, R.-S. Liu, C.-P. Han, Y. Li, Y. Gogotsi, G. Wang, Single platinum atoms immobilized on an MXene as an efficient catalyst for the hydrogen evolution reaction, Nat. Catal. 1 (2018) 985–992. https://doi.org/10.1038/s41929-018-0195-1.

585 [13] B. Wei, Z. Fu, D. Legut, T.C. Germann, S. Du, H. Zhang, J.S. Francisco, R. Zhang, Rational Design of
586   Highly Stable and Active MXene-Based Bifunctional ORR/OER Double-Atom Catalysts, Adv. Mater.
587   33 (2021) 2102595. https://doi.org/10.1002/adma.202102595.

588 [14] W.-J. Niu, J.-Z. He, B.-N. Gu, M.-C. Liu, Y.-L. Chueh, Opportunities and Challenges in Precise
589   Synthesis of Transition Metal Single-Atom Supported by 2D Materials as Catalysts toward Oxygen
590   Reduction Reaction, Adv. Funct. Mater. 31 (2021) 2103558.
591   https://doi.org/10.1002/adfm.202103558.

592 [15] K.E. Fritz, Y. Yan, J. Suntivich, Influence of 3d transition-metal substitution on the oxygen reduction
593   reaction electrocatalysis of ternary nitrides in acid, Nano Res. 12 (2019) 2307–2312.
594   https://doi.org/10.1007/s12274-019-2440-6.

595 [16] M.E. Kreider, A. Gallo, S. Back, Y. Liu, S. Siahrostami, D. Nordlund, R. Sinclair, J.K. Nørskov, L.A.
596   King, T.F. Jaramillo, Precious Metal-Free Nickel Nitride Catalyst for the Oxygen Reduction Reaction,
597   ACS Appl. Mater. Interfaces. 11 (2019) 26863–26871. https://doi.org/10.1021/acsami.9b07116.

598 [17] C. Goswami, K.K. Hazarika, P. Bharali, Transition metal oxide nanocatalysts for oxygen reduction
599   reaction, Mater. Sci. Energy Technol. 1 (2018) 117–128.
600   https://doi.org/10.1016/j.mset.2018.06.005.

601 [18] T. Sun, Y. Jiang, Q. Wu, L. Du, Z. Zhang, L. Yang, X. Wang, Z. Hu, Is iron nitride or carbide highly
602   active for oxygen reduction reaction in acidic medium?, Catal. Sci. Technol. 7 (2017) 51–55.
603   https://doi.org/10.1039/C6CY01921H.

604 [19] F. Li, G.-F. Han, H.-J. Noh, S.-J. Kim, Y. Lu, H.Y. Jeong, Z. Fu, J.-B. Baek, Boosting oxygen reduction
605   catalysis with abundant copper single atom active sites, Energy Environ. Sci. 11 (2018) 2263–2269.
606   https://doi.org/10.1039/C8EE01169A.

607 [20] Y. Wang, H. Yuan, Y. Li, Z. Chen, Two-dimensional iron-phthalocyanine (Fe-Pc) monolayer as a
608   promising single-atom-catalyst for oxygen reduction reaction: a computational study, Nanoscale. 7
609   (2015) 11633–11641. https://doi.org/10.1039/C5NR00302D.

610 [21] L. Yang, S. Jiang, Y. Zhao, L. Zhu, S. Chen, X. Wang, Q. Wu, J. Ma, Y. Ma, Z. Hu, Boron-Doped Carbon
611   Nanotubes as Metal-Free Electrocatalysts for the Oxygen Reduction Reaction, Angew. Chem. Int.
612   Ed. 50 (2011) 7132–7135. https://doi.org/10.1002/anie.201101287.

613 [22] D. Guo, R. Shibuya, C. Akiba, S. Saji, T. Kondo, J. Nakamura, Active sites of nitrogen-doped carbon
614   materials for oxygen reduction reaction clarified using model catalysts, Science. 351 (2016) 361–
615   365. https://doi.org/10.1126/science.aad0832.

616 [23] L. Peles-Strahl, N. Zion, O. Lori, N. Levy, G. Bar, A. Dahan, L. Elbaz, Bipyridine Modified Conjugated
617   Carbon Aerogels as a Platform for the Electrocatalysis of Oxygen Reduction Reaction, Adv. Funct.
618   Mater. 31 (2021) 2100163. https://doi.org/10.1002/adfm.202100163.

619 [24] Z. Zhang, J. Sun, F. Wang, L. Dai, Efficient Oxygen Reduction Reaction (ORR) Catalysts Based on
620   Single Iron Atoms Dispersed on a Hierarchically Structured Porous Carbon Framework, Angew.
621   Chem. 130 (2018) 9176–9181. https://doi.org/10.1002/ange.201804958.

622 [25] H. Fei, J. Dong, Y. Feng, C.S. Allen, C. Wan, B. Volosskiy, M. Li, Z. Zhao, Y. Wang, H. Sun, P. An, W.
623   Chen, Z. Guo, C. Lee, D. Chen, I. Shakir, M. Liu, T. Hu, Y. Li, A.I. Kirkland, X. Duan, Y. Huang, General
624   synthesis and definitive structural identification of MN4C4 single-atom catalysts with tunable
625   electrocatalytic activities, Nat. Catal. 1 (2018) 63–72. https://doi.org/10.1038/s41929-017-0008-y.

626 [26] S. An, G. Zhang, T. Wang, W. Zhang, K. Li, C. Song, J.T. Miller, S. Miao, J. Wang, X. Guo, High-Density
627   Ultra-small Clusters and Single-Atom Fe Sites Embedded in Graphitic Carbon Nitride (g-C3N4) for
628   Highly Efficient Catalytic Advanced Oxidation Processes, ACS Nano. 12 (2018) 9441–9450.
629   https://doi.org/10.1021/acsnano.8b04693.

630   [27]   Q. Liu, Q. Li, S. Chen, Metal–nitrogen coordination moieties in carbon for effective electrocatalytic
631   reduction of oxygen, Curr. Opin. Electrochem. 21 (2020) 46–54.
632   https://doi.org/10.1016/j.coelec.2020.01.002.

633   [28]   H.B. Yang, J. Miao, S.-F. Hung, J. Chen, H.B. Tao, X. Wang, L. Zhang, R. Chen, J. Gao, H.M. Chen, L.
634   Dai, B. Liu, Identification of catalytic sites for oxygen reduction and oxygen evolution in N-doped
635   graphene materials: Development of highly efficient metal-free bifunctional electrocatalyst, Sci.
636   Adv. 2 (2016) e1501122. https://doi.org/10.1126/sciadv.1501122.

637   [29]   L. Yang, D. Cheng, H. Xu, X. Zeng, X. Wan, J. Shui, Z. Xiang, D. Cao, Unveiling the high-activity origin
638   of single-atom iron catalysts for oxygen reduction reaction, Proc. Natl. Acad. Sci. 115 (2018) 6626–
639   6631. https://doi.org/10.1073/pnas.1800771115.

640   [30]   J. Wang, R. Xu, Y. Li, Y. Li, M. Yang, G. Yang, Y. Zhao, F. Gao, Recent progress, developing strategies,
641   theoretical insights, and perspectives towards high-performance copper single atom
642   electrocatalysts, Mater. Today Energy. 21 (2021) 100761.
643   https://doi.org/10.1016/j.mtener.2021.100761.

644   [31]   W. Li, C. Min, F. Tan, Z. Li, B. Zhang, R. Si, M. Xu, W. Liu, L. Zhou, Q. Wei, Y. Zhang, X. Yang, Bottom-
645   Up Construction of Active Sites in a Cu–N4–C Catalyst for Highly Efficient Oxygen Reduction
646   Reaction, ACS Nano. 13 (2019) 3177–3187. https://doi.org/10.1021/acsnano.8b08692.

647   [32]   E. Jung, H. Shin, B.-H. Lee, V. Efremov, S. Lee, H.S. Lee, J. Kim, W. Hooch Antink, S. Park, K.-S. Lee,
648   S.-P. Cho, J.S. Yoo, Y.-E. Sung, T. Hyeon, Atomic-level tuning of Co–N–C catalyst for high-
649   performance electrochemical H2O2 production, Nat. Mater. 19 (2020) 436–442.
650   https://doi.org/10.1038/s41563-019-0571-5.

651   [33]   Y. Wang, R. Shi, L. Shang, G.I.N. Waterhouse, J. Zhao, Q. Zhang, L. Gu, T. Zhang, High-Efficiency
652   Oxygen Reduction to Hydrogen Peroxide Catalyzed by Nickel Single-Atom Catalysts with
653   Tetradentate N2O2 Coordination in a Three-Phase Flow Cell, Angew. Chem. Int. Ed. 59 (2020)
654   13057–13062. https://doi.org/10.1002/anie.202004841.

655   [34]   Z. Chen, X. Fan, Z. Shen, X. Ruan, L. Wang, H. Zeng, J. Wang, Y. An, Y. Hu, Cu Anchored Ti2NO2 as
656   High Performance Electrocatalyst for Oxygen Evolution Reaction: A Density Functional Theory
657   Study, ChemCatChem. 12 (2020) 4059–4066. https://doi.org/10.1002/cctc.202000591.

658   [35]   Y. Wen, C. Ma, Z. Wei, X. Zhu, Z. Li, FeNC/MXene hybrid nanosheet as an efficient electrocatalyst
659   for oxygen reduction reaction, RSC Adv. 9 (2019) 13424–13430.
660   https://doi.org/10.1039/C9RA01330J.

661   [36]   L. Chen, Y. Lin, J. Fu, J. Xie, R. Chen, H. Zhang, Hybridization of Binary Non-Precious-Metal
662   Nanoparticles with d-Ti3C2 MXene for Catalyzing the Oxygen Reduction Reaction,
663   ChemElectroChem. 5 (2018) 3307–3314. https://doi.org/10.1002/celc.201800693.

664   [37]   M. Yu, S. Zhou, Z. Wang, J. Zhao, J. Qiu, Boosting electrocatalytic oxygen evolution by
665   synergistically coupling layered double hydroxide with MXene, Nano Energy. 44 (2018) 181–190.
666   https://doi.org/10.1016/j.nanoen.2017.12.003.

667   [38]   Q. Xue, Z. Pei, Y. Huang, M. Zhu, Z. Tang, H. Li, Y. Huang, N. Li, H. Zhang, C. Zhi, Mn3O4
668   nanoparticles on layer-structured Ti3C2 MXene towards the oxygen reduction reaction and zinc–
669   air batteries, J. Mater. Chem. A. 5 (2017) 20818–20823. https://doi.org/10.1039/C7TA04532H.

670   [39]   L. Jiang, J. Duan, J. Zhu, S. Chen, M. Antonietti, Iron-Cluster-Directed Synthesis of 2D/2D Fe–N–
671   C/MXene Superlattice-like Heterostructure with Enhanced Oxygen Reduction Electrocatalysis, ACS
672   Nano. 14 (2020) 2436–2444. https://doi.org/10.1021/acsnano.9b09912.

673   [40]   M. Keyhanian, D. Farmanzadeh, Á. Morales-García, F. Illas, Effect of oxygen termination on the
674   interaction of first row transition metals with M2C MXenes and the feasibility of single-atom
675   catalysts, J. Mater. Chem. A. 10 (2022) 8846–8855. https://doi.org/10.1039/D1TA10252D.

676 [41] Y. Wen, Z. Wei, C. Ma, X. Xing, Z. Li, D. Luo, MXene Boosted CoNi-ZIF-67 as Highly Efficient
677   Electrocatalysts for Oxygen Evolution, Nanomaterials. 9 (2019) 775.
678   https://doi.org/10.3390/nano9050775.

679 [42] X. Zhao, H. Xu, Z. Hui, Y. Sun, C. Yu, J. Xue, R. Zhou, L. Wang, H. Dai, Y. Zhao, J. Yang, J. Zhou, Q.
680   Chen, G. Sun, W. Huang, Electrostatically Assembling 2D Nanosheets of MXene and MOF-
681   Derivatives into 3D Hollow Frameworks for Enhanced Lithium Storage, Small. 15 (2019) 1904255.
682   https://doi.org/10.1002/smll.201904255.

683 [43] L. Zhao, B. Dong, S. Li, L. Zhou, L. Lai, Z. Wang, S. Zhao, M. Han, K. Gao, M. Lu, X. Xie, B. Chen, Z. Liu,
684   X. Wang, H. Zhang, H. Li, J. Liu, H. Zhang, X. Huang, W. Huang, Interdiffusion Reaction-Assisted
685   Hybridization of Two-Dimensional Metal–Organic Frameworks and Ti3C2Tx Nanosheets for
686   Electrocatalytic Oxygen Evolution, ACS Nano. 11 (2017) 5800–5807.
687   https://doi.org/10.1021/acsnano.7b01409.

688 [44] X. Liang, X. Ren, Q. Yang, L. Gao, M. Gao, Y. Yang, H. Zhu, G. Li, T. Ma, A. Liu, A two-dimensional
689   MXene-supported metal–organic framework for highly selective ambient electrocatalytic nitrogen
690   reduction, Nanoscale. 13 (2021) 2843–2848. https://doi.org/10.1039/D0NR08744K.

691 [45] C.-F. Du, Q. Song, Q. Liang, X. Zhao, J. Wang, R. Zhi, Y. Wang, H. Yu, The Passive Effect of MXene on
692   Electrocatalysis: A Case of Ti3C2Tx/CoNi–MOF nanosheets for Oxygen Evolution Reaction,
693   ChemNanoMat. 7 (2021) 539–544. https://doi.org/10.1002/cnma.202100061.

694 [46] H. Zou, B. He, P. Kuang, J. Yu, K. Fan, Metal–Organic Framework-Derived Nickel–Cobalt Sulfide on
695   Ultrathin Mxene Nanosheets for Electrocatalytic Oxygen Evolution, ACS Appl. Mater. Interfaces. 10
696   (2018) 22311–22319. https://doi.org/10.1021/acsami.8b06272.

697 [47] H. Zhang, Z. Li, Z. Hou, H. Mei, Y. Feng, B. Xu, D. Sun, Self-assembly of MOF on MXene nanosheets
698   and in-situ conversion into superior nickel phosphates/MXene battery-type electrode, Chem. Eng.
699   J. 425 (2021) 130602. https://doi.org/10.1016/j.cej.2021.130602.

700 [48] P. Chen, Y. Tong, C. Wu, Y. Xie, Surface/Interfacial Engineering of Inorganic Low-Dimensional
701   Electrode Materials for Electrocatalysis, Acc. Chem. Res. 51 (2018) 2857–2866.
702   https://doi.org/10.1021/acs.accounts.8b00266.

703 [49] C. Zhu, S. Fu, Q. Shi, D. Du, Y. Lin, Single-Atom Electrocatalysts, Angew. Chem. Int. Ed. 56 (2017)
704   13944–13960. https://doi.org/10.1002/anie.201703864.

705 [50] Y. Qu, Z. Li, W. Chen, Y. Lin, T. Yuan, Z. Yang, C. Zhao, J. Wang, C. Zhao, X. Wang, F. Zhou, Z. Zhuang,
706   Y. Wu, Y. Li, Direct transformation of bulk copper into copper single sites via emitting and trapping
707   of atoms, Nat. Catal. 1 (2018) 781–786. https://doi.org/10.1038/s41929-018-0146-x.

708 [51] Z. Shi, J. Liu, T. Lin, F. Xia, P.N. Liu, N. Lin, Thermodynamics and Selectivity of Two-Dimensional
709   Metallo-supramolecular Self-Assembly Resolved at Molecular Scale, J. Am. Chem. Soc. 133 (2011)
710   6150–6153. https://doi.org/10.1021/ja2010434.

711 [52] J. Liu, T. Lin, Z. Shi, F. Xia, L. Dong, P.N. Liu, N. Lin, Structural Transformation of Two-Dimensional
712   Metal–Organic Coordination Networks Driven by Intrinsic In-Plane Compression, J. Am. Chem. Soc.
713   133 (2011) 18760–18766. https://doi.org/10.1021/ja2056193.

714 [53] X. Zhang, M. Zhao, Robust half-metallicity and topological aspects in two-dimensional Cu-TPyB, Sci.
715   Rep. 5 (2015) 14098. https://doi.org/10.1038/srep14098.

716 [54] A.I. Fadeeva, V.A. Gorbunov, O.S. Solovyeva, P.V. Stishenko, A.V. Myshlyavtsev, Homologous Series
717   of Flower Phases in Metal–Organic Networks on Au(111) Surface, J. Phys. Chem. C. 124 (2020)
718   11506–11515. https://doi.org/10.1021/acs.jpcc.0c02527.

719 [55] J. Rodríguez-Fernández, Y. Wang, M. Alcamí, F. Martín, R. Otero, J.M. Gallego, R. Miranda, Thermal
720 Transition from a Disordered, 2D Network to a Regular, 1D, Fe(II)–DCNQI Coordination Network, J.
721 Phys. Chem. C. 120 (2016) 16712–16721. https://doi.org/10.1021/acs.jpcc.6b04288.

722 [56] Y. Song, Y. Wang, Q. Jin, K. Zhou, Z. Shi, P.-N. Liu, Y. Ma, Self-Assembly and Local Manipulation of
723 Au-Pyridyl Coordination Networks on Metal Surfaces, ChemPhysChem. 18 (2017) 2088–2093.
724 https://doi.org/10.1002/cphc.201700439.

725 [57] D. Nieckarz, P. Szabelski, Understanding Pattern Formation in 2D Metal–Organic Coordination
726 Systems on Solid Surfaces, J. Phys. Chem. C. 117 (2013) 11229–11241.
727 https://doi.org/10.1021/jp4022486.

728 [58] D. Ecija, M. Marschall, J. Reichert, A. Kasperski, D. Nieckarz, P. Szabelski, W. Auwärter, J.V. Barth,
729 Dynamics and thermal stability of surface-confined metal–organic chains, Surf. Sci. 643 (2016) 91–
730 97. https://doi.org/10.1016/j.susc.2015.08.013.

731 [59] K. Gdula, D. Nieckarz, On-Surface Self-Assembly of Metal-Organic Architectures: Insights from
732 Computer Simulations, J. Phys. Chem. C. 124 (2020) 20066–20078.
733 https://doi.org/10.1021/acs.jpcc.0c04597.

734 [60] A.I. Fadeeva, V.A. Gorbunov, P.V. Stishenko, A.V. Myshlyavtsev, Model of Fe-Terephthalate
735 Ordering on Cu(100), J. Phys. Chem. C. 123 (2019) 17265–17272.
736 https://doi.org/10.1021/acs.jpcc.9b02834.

737 [61] J. Lisiecki, P. Szabelski, Surface-Confined Metal–Organic Precursors Comprising Naphthalene-Like
738 Derivatives with Differently Distributed Halogen Substituents: A Monte Carlo Model, J. Phys.
739 Chem. C. 124 (2020) 20280–20293. https://doi.org/10.1021/acs.jpcc.0c06726.

740 [62] A.I. Fadeeva, V.A. Gorbunov, P.V. Stishenko, S.S. Akimenko, A.V. Myshlyavtsev, Melting of Fe-
741 terephthalate layers on Cu(1 0 0) surface with randomly distributed point defects, Appl. Surf. Sci.
742 545 (2021) 148989. https://doi.org/10.1016/j.apsusc.2021.148989.

743 [63] J. Lisiecki, P. Szabelski, Halogenated Anthracenes as Building Blocks for the On-Surface Synthesis of
744 Covalent Polymers: Structure Prediction with the Lattice Monte Carlo Method, J. Phys. Chem. C.
745 125 (2021) 15934–15949. https://doi.org/10.1021/acs.jpcc.1c03973.

746 [64] B. Delley, From molecules to solids with the DMol3 approach, J. Chem. Phys. 113 (2000) 7756–
747 7764. https://doi.org/10.1063/1.1316015.

748 [65] B. Hammer, L.B. Hansen, J.K. Nørskov, Improved adsorption energetics within density-functional
749 theory using revised Perdew-Burke-Ernzerhof functionals, Phys. Rev. B. 59 (1999) 7413–7421.
750 https://doi.org/10.1103/PhysRevB.59.7413.

751 [66] B. Delley, An all-electron numerical method for solving the local density functional for polyatomic
752 molecules, J. Chem. Phys. 92 (1990) 508–517. https://doi.org/10.1063/1.458452.

753 [67] B. Delley, Ground-State Enthalpies: Evaluation of Electronic Structure Approaches with Emphasis
754 on the Density Functional Method, J. Phys. Chem. A. 110 (2006) 13632–13639.
755 https://doi.org/10.1021/jp0653611.

756 [68] M. Dolg, U. Wedig, H. Stoll, H. Preuss, Energy-adjusted ab initio pseudopotentials for the first row
757 transition elements, J. Chem. Phys. 86 (1987) 866–872. https://doi.org/10.1063/1.452288.

758 [69] A. Bergner, M. Dolg, W. Küchle, H. Stoll, H. Preuß, Ab initio energy-adjusted pseudopotentials for
759 elements of groups 13–17, Mol. Phys. 80 (1993) 1431–1441.
760 https://doi.org/10.1080/00268979300103121.

761 [70] A. Tkatchenko, M. Scheffler, Accurate Molecular Van Der Waals Interactions from Ground-State
762 Electron Density and Free-Atom Reference Data, Phys. Rev. Lett. 102 (2009) 073005.
763 https://doi.org/10.1103/PhysRevLett.102.073005.

764 [71] E.R. McNellis, J. Meyer, K. Reuter, Azobenzene at coinage metal surfaces: Role of dispersive van
765   der Waals interactions, Phys. Rev. B. 80 (2009) 205414.
766   https://doi.org/10.1103/PhysRevB.80.205414.

767 [72] M.A. Caro, Parametrization of the Tkatchenko-Scheffler dispersion correction scheme for popular
768   exchange-correlation density functionals: effect on the description of liquid water,
769   ArXiv170400761 Cond-Mat. (2017). http://arxiv.org/abs/1704.00761 (accessed November 12,
770   2021).

771 [73] M. Methfessel, A.T. Paxton, High-precision sampling for Brillouin-zone integration in metals, Phys.
772   Rev. B. 40 (1989) 3616–3621. https://doi.org/10.1103/PhysRevB.40.3616.

773 [74] P. Pulay, Convergence acceleration of iterative sequences. the case of scf iteration, Chem. Phys.
774   Lett. 73 (1980) 393–398. https://doi.org/10.1016/0009-2614(80)80396-4.

775 [75] Y. Jiang, T. Sun, X. Xie, W. Jiang, J. Li, B. Tian, C. Su, Oxygen-Functionalized Ultrathin Ti3C2Tx
776   MXene for Enhanced Electrocatalytic Hydrogen Evolution, ChemSusChem. 12 (2019) 1368–1373.
777   https://doi.org/10.1002/cssc.201803032.

778 [76] J.D. Gouveia, G. Novell-Leruth, P.M.L.S. Reis, F. Viñes, F. Illas, J.R.B. Gomes, First-Principles
779   Calculations on the Adsorption Behavior of Amino Acids on a Titanium Carbide MXene, ACS Appl.
780   Bio Mater. 3 (2020) 5913–5921. https://doi.org/10.1021/acsabm.0c00621.

781 [77] J.D. Gouveia, G. Novell-Leruth, F. Viñes, F. Illas, J.R.B. Gomes, The Ti2CO2 MXene as a nucleobase
782   2D sensor: A first-principles study, Appl. Surf. Sci. 544 (2021) 148946.
783   https://doi.org/10.1016/j.apsusc.2021.148946.

784 [78] J.M. Soler, E. Artacho, J.D. Gale, A. García, J. Junquera, P. Ordejón, D. Sánchez-Portal, The SIESTA
785   method forab initioorder-Nmaterials simulation, J. Phys. Condens. Matter. 14 (2002) 2745–2779.
786   https://doi.org/10.1088/0953-8984/14/11/302.

787 [79] E. Caldeweyher, C. Bannwarth, S. Grimme, Extension of the D3 dispersion coefficient model, J.
788   Chem. Phys. 147 (2017) 034112. https://doi.org/10.1063/1.4993215.

789 [80] E. Caldeweyher, S. Ehlert, A. Hansen, H. Neugebauer, S. Spicher, C. Bannwarth, S. Grimme, A
790   generally applicable atomic-charge dependent London dispersion correction, J. Chem. Phys. 150
791   (2019) 154122. https://doi.org/10.1063/1.5090222.

792 [81] S. Alvarez, A cartography of the van der Waals territories, Dalton Trans. 42 (2013) 8617–8636.
793   https://doi.org/10.1039/C3DT50599E.

794 [82] SuSMoST, https://susmost.com/ (accessed November 12, 2021).

795 [83] SuSMoST / Models, GitLab. https://gitlab.com/susmost/models (accessed November 12, 2021).

796 [84] S.S. Akimenko, G.D. Anisimova, A.I. Fadeeva, V.F. Fefelov, V.A. Gorbunov, T.R. Kayumova, A.V.
797   Myshlyavtsev, M.D. Myshlyavtseva, P.V. Stishenko, SuSMoST: Surface Science Modeling and
798   Simulation Toolkit, J. Comput. Chem. 41 (2020) 2084–2097. https://doi.org/10.1002/jcc.26370.

799 [85] D.P. Landau, K. Binder, A guide to Monte Carlo simulations in statistical physics, Fourth edition,
800   Cambridge University Press, Cambridge, United Kingdom, 2015.

801 [86] D. J. Earl, M. W. Deem, Parallel tempering: Theory, applications, and new perspectives, Phys.
802   Chem. Chem. Phys. 7 (2005) 3910–3916. https://doi.org/10.1039/B509983H.

803